

# Three-Dimensional Quantitative Co-Mapping of Pulmonary Morphology and Nanoparticle Distribution with Cellular Resolution in Nondissected Murine Lungs

Lin Yang,<sup>†,‡,||</sup> Annette Feuchtinger,<sup>§</sup> Winfried Möller,<sup>†,‡</sup> Yaobo Ding,<sup>†,‡</sup> David Kutschke,<sup>†,‡</sup> Gabriele Möller,<sup>#</sup> Johannes C. Schittny,<sup>¶</sup> Gerald Burgstaller,<sup>†,‡</sup> Werner Hofmann,<sup>□</sup> Tobias Stoeger,<sup>†,‡</sup> Daniel Razansky,<sup>||</sup> Alex Walch,<sup>§</sup> and Otmar Schmid<sup>\*,†,‡</sup>

<sup>†</sup>Comprehensive Pneumology Center (CPC-M), Member of the German Center for Lung Research (DZL), Munich, 81377, Germany

<sup>‡</sup>Institute of Lung Biology and Disease, Helmholtz Zentrum München—German Research Center for Environmental Health, Neuherberg, 85764, Germany

<sup>§</sup>Research Unit Analytical Pathology, Helmholtz Zentrum München, Neuherberg, 85764, Germany

<sup>¶</sup>Institute for Biological and Medical Imaging (IBMI), Helmholtz Zentrum München, Neuherberg, 85764, Germany

<sup>#</sup>Faculty of Medicine, Technical University of Munich, Munich, 80333, Germany

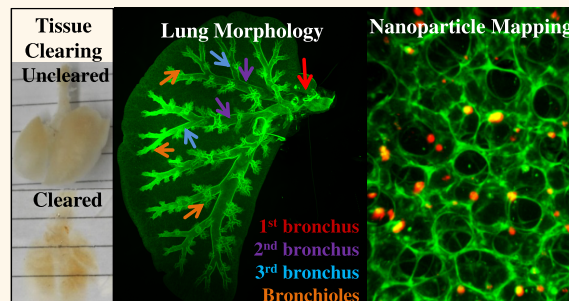
<sup>\*</sup>Department Genome Analysis Center, Institute of Experimental Genetics, Helmholtz Zentrum München, Neuherberg, 85764, Germany

<sup>¶</sup>Institute of Anatomy, University of Bern, CH-3012 Bern, Switzerland

<sup>□</sup>Department of Chemistry and Physics of Materials, University of Salzburg, Salzburg, A-5020, Austria

## Supporting Information

**ABSTRACT:** Deciphering biodistribution, biokinetics, and biological effects of nanoparticles (NPs) in entire organs with cellular resolution remains largely elusive due to the lack of effective imaging tools. Here, light sheet fluorescence microscopy in combination with optical tissue clearing was validated for concomitant three-dimensional mapping of lung morphology and NP biodistribution with cellular resolution in nondissected *ex vivo* murine lungs. Tissue autofluorescence allowed for label-free, quantitative morphometry of the entire bronchial tree, acinar structure, and blood vessels. Co-registration of fluorescent NPs with lung morphology revealed significant differences in pulmonary NP distribution depending on the means of application (intratracheal instillation and ventilator-assisted aerosol inhalation under anesthetized conditions). Inhalation exhibited a more homogeneous NP distribution in conducting airways and acini indicated by a central-to-peripheral (C/P) NP deposition ratio of unity ( $0.98 \pm 0.13$ ) as compared to a 2-fold enhanced central deposition ( $C/P = 1.98 \pm 0.37$ ) for instillation. After inhalation most NPs were observed in the proximal part of the acini as predicted by computational fluid dynamics simulations. At cellular resolution patchy NP deposition was visualized in bronchioles and acini, but more pronounced for instillation. Excellent linearity of the fluorescence intensity–dose response curve allowed for accurate NP dosimetry and revealed *ca.* 5% of the inhaled aerosol was deposited in the lungs. This single-modality imaging technique allows for quantitative co-registration of tissue architecture and NP biodistribution, which could accelerate elucidation of NP biokinetics and bioactivity within intact tissues, facilitating both nanotoxicology studies and the development of nanomedicines.



**KEYWORDS:** 3D whole lung imaging, pulmonary nanoparticle delivery, 3DISCO, optical tissue clearing, acinar deposition, airway deposition

The superb physicochemical properties of manufactured nanomaterials (NMs) greatly facilitate their increasingly widespread use in medicine and industry, which has led to exponential growth of NM-containing industrial

Received: October 2, 2018

Accepted: December 19, 2018

Published: December 19, 2018

products over the past decades.<sup>1,2</sup> Large-scale manufacturing of NMs substantially increased the risks for human health especially but not limited to occupational settings,<sup>3</sup> resulting in the release of new guidelines by the World Health Organization (WHO) to protect workers from the potential risks of NMs.<sup>4</sup> In particular, respiratory inhalation of NMs and/or nanosized ambient particulate matter is a major public concern mainly associated with cardiovascular and pulmonary morbidity and mortality.<sup>5,6</sup> Meanwhile, a number of novel-designed nanomaterial-based drugs (nanomedicines such as liposomes and polymers) are currently being evaluated at the preclinical level or have even reached the clinical settings.<sup>7–9</sup> Consequently, extensive scientific efforts have been focused on understanding the fate of NMs in the organism and the underlying pathomechanisms of disease (or diagnostic and therapeutic effects) after respiratory delivery of NMs.<sup>10,11</sup>

Intratracheal instillation and inhalation of NMs was most widely used in animal and human studies on the fate and toxicity of NMs.<sup>11–13</sup> NMs were proved to be able to reach deep into the lung alveolar region and translocate from the lungs to circulation and from there to secondary organs, resulting in dose-dependent oxidative stress and inflammation, which often scales well with organ-delivered surface area dose.<sup>14–16</sup> Most of these studies have been performed with spherical NMs, henceforth referred to as nanoparticles (NPs). Inhaled gold NPs were preferentially found at sites of vascular inflammation in both diseased rodents and humans examined using high-resolution inductively coupled plasma mass spectroscopy (ICP-MS) and Raman microscopy.<sup>17</sup> Thus, distribution, localization, and dosimetry of NPs within whole organs and even whole organisms are of paramount importance for understanding the link between physicochemical characteristics of NPs and associated health effects.<sup>18–20</sup> Currently available *in vivo* imaging techniques offer gross anatomical distribution of NPs using, for example, X-ray computed tomography, magnetic resonance imaging (MRI), *in vivo* imaging system (IVIS), positron emission tomography (PET), single photon emission computed tomography (SPECT), and photoacoustic imaging.<sup>2,9</sup> However, these modalities are often unable to resolve biological interactions of NPs with tissue and are limited to visualizing NP localization at cellular resolution. To achieve this goal, several common *ex vivo* assays, including transmission electron microscopy (TEM), 2D stereological methods, flow cytometry, and ICP-MS, were applied to examine and/or quantify NP localization and distribution at cellular resolution, but the information on 3D tissue architecture was totally destroyed.<sup>20–22</sup> Currently, no available technique is able to both visualize the spatial distribution of NPs and quantify their accumulated dose in entire organs (*e.g.*, lungs) with cellular resolution.

Moreover, understanding the spatial distribution and biokinetics of NPs with cellular resolution at the whole organ level has also significant implications for NP-based drug delivery (*e.g.*, nanomedicines).<sup>8,23</sup> For instance, the delivery of nanomedicines into diseased regions of the lungs *via* inhalation is of central importance for therapeutic efficacy and pharmacokinetics. 3D imaging of whole diseased organs could provide both qualitative and quantitative data on nanomedicine delivery to the sites of disease (*e.g.*, lung cancer or alveolar region for the treatment of lung emphysema), and thus verify the targeting efficacy of novel-designed nanomedicines.<sup>2,9,24</sup>

As mentioned above, current imaging methods with cellular resolution rely on tissue sectioning. Alternatively, in order to observe the 3D imaging maintaining the integrity of tissue

architecture, tissues ideally should be imaged as a whole organ or whole body without sectioning. However, biological tissues generally have strong light absorption and light scattering, which hamper light penetration, leading to low resolution and imaging depth.<sup>25</sup> Recently, the concept of optical tissue clearing attracted major interest, as it essentially renders tissues transparent, enabling 3D imaging of intact tissue using confocal laser microscopy and two-photon microscopy.<sup>25,26</sup> The more recent emergence of light sheet fluorescence microscopy (LSFM) has revolutionized several fields of research, primarily neurobiology and embryology, since this 3D imaging method allows unraveling of molecular and cellular events at the whole organ level (*e.g.*, the brain and embryo).<sup>27,28</sup> Allowing multiwavelength imaging of endogenous fluorescence proteins, immune-labeled biomolecules, and intravenously delivered probes, LSFM permits 3D imaging of tissue structure such as vascular system, neurons, axons, glomerulus, *etc.*, offering more accurate data of tissue morphology and physiological or pathological state compared to the traditional 2D histomorphological method.<sup>29,30</sup> High scattering effects in the lung due to the millions of air–tissue interfaces have made the lung a particularly elusive inner organ for LSFM even for small rodent models (mice). Hence, unlike the liver and spleen, there are currently no LSFM data on co-registration of 3D lung morphology and quantitative NP distribution throughout the entire murine lung.<sup>31</sup>

This study aims to co-register the lung architecture and quantitative distribution of pulmonary applied NPs in non-dissected (whole) and unstained murine lungs by using LSFM after 3DISCO<sup>25</sup> tissue clearing (as a time-saving and high-quality clearing method). This study provides a label-free 3D visualization and morphometric analysis of the complete epithelial architecture of an entire murine lung combined with quantitative dosimetry of fluorescently labeled NPs at the whole-organ level with cellular resolution. This revealed insights into the effect of different routes of NP application (intratracheal instillation and inhalation) on the pulmonary NP deposition profile.

## RESULTS

The method presented here allows for simultaneous 3D mapping of label-free lung morphology and pulmonary distribution of fluorescent NPs. This requires bichannel imaging of optically cleared lungs with one channel optimized for tissue autofluorescence and the other tailored toward the fluorescence spectrum of the NPs under investigation.

**3D Visualization and Quantitative Analysis of Whole Lung Morphology.** 3D lung morphology and airway architecture were generated from tissue autofluorescence imaged using the excitation and emission (ex/em) filters at 545 and 605 nm, respectively. The degree of transparency of a cleared lung after undergoing the refined 3DISCO protocol is evident from Figure 1a. An example of selected images obtained from sequential planewise illumination of the whole lung using LSFM is depicted in Figure 1b. 3D reconstruction of the entire stack of images allowed for clear identification of the entire airway structure down to generation 16 to 21 and even beyond into the alveolar structure and blood vessels (Figure 1c and Video S1). To categorize the airway segments of the monopodial lung structure of a mouse, an “order”-based terminology as introduced by Wallau *et al.*<sup>32</sup> is more suitable than generation-based numbering schemes, which are more suitable for dichotomous lungs (*e.g.*, from humans). In an order-based lung structure, a daughter airway segment can be assigned

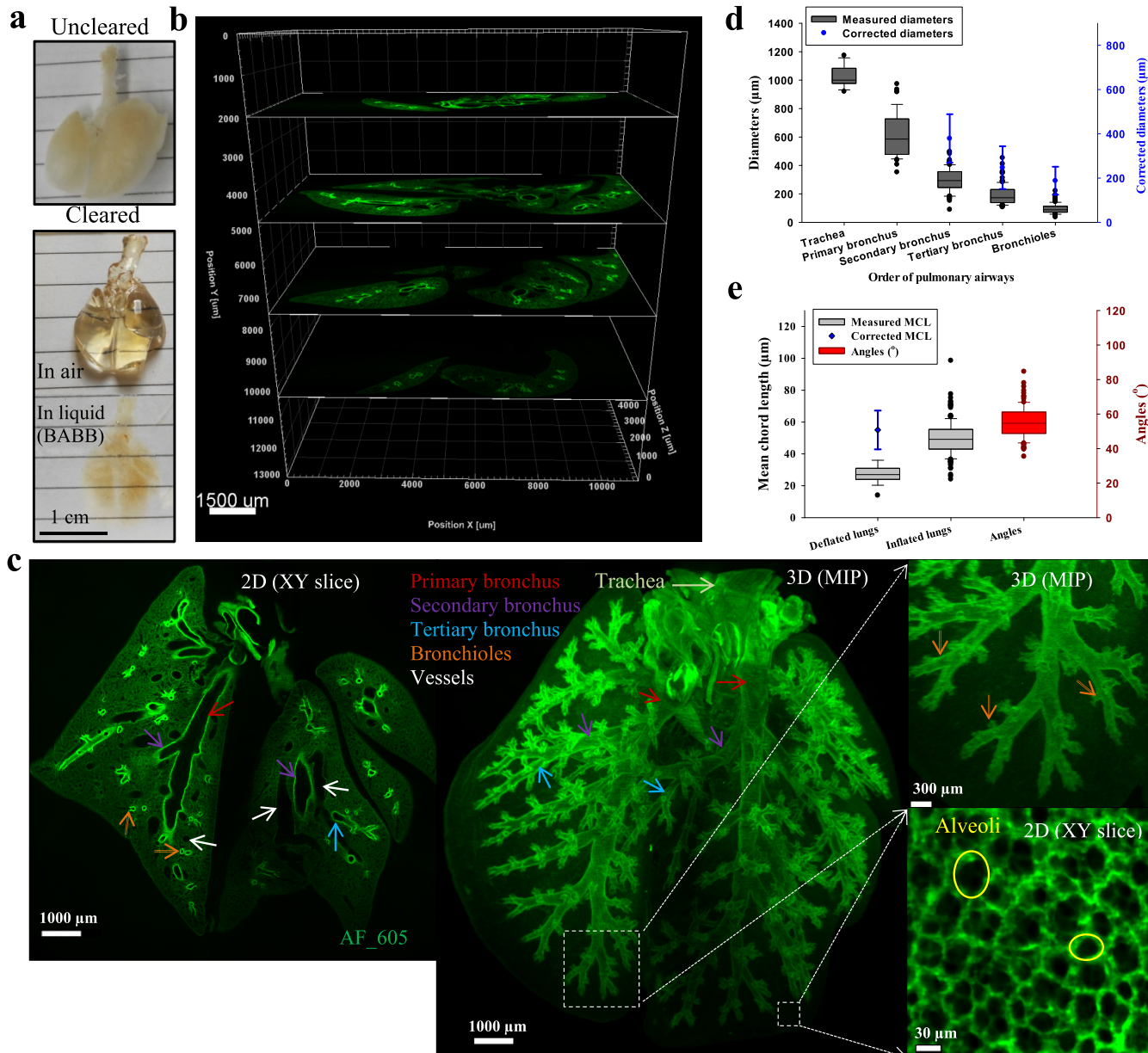


**Figure 1.** Three-dimensional (3D) visualization and quantitative morphometry of a whole murine lung using light sheet fluorescence microscopy (LSFM) after tissue clearing in the tissue autofluorescence channel ( $\text{ex}/\text{em} = 545/605 \text{ nm}$ ). (a) Whole mouse lung prior to (uncleared) and after tissue clearing (in air and in BABB solvent). (b) Z-stack of sequential images recorded as the lung is illuminated *via* stepwise-shifted light sheets along the Z-dimension. The resulting images cover the entire width of the lung ( $>1 \text{ cm}$ ) with no loss of image quality near the center, the point of maximum light attenuation. (c) Representative images of a single (2D) light sheet and a 3D reconstruction of the whole lung using maximum intensity projection over the entire image stack, which clearly exhibit the full anatomical information from the trachea, over the primary bronchus down to the small (terminal) bronchioles and even the blood vessels. The typical alveolar honeycomb structure can also be visualized when imaging at cellular resolution using LSFM. (d) Originally measured and deflation- and shrinkage-corrected (3D) diameters of the branches of the pulmonary bronchial tree (from trachea to small bronchioles) are presented. (e) Originally measured and (deflation-/shrinkage-) corrected mean chord lengths (MCL) of the alveolar region, as well as the branching angles of the entire bronchial tree in deflated lungs, and MCL in inflated lungs (no deflation-/shrinkage-correction as the lung was filled with agar) are displayed.

the same order as its parent segment if its diameter is closer to that of its parent segment or significantly larger than its sister segments. Otherwise, all daughter segments receive an order greater than that of their parent segment (Figure 1c). Of note, the original distribution of NPs is expected to be preserved in deflated or unfilled lungs, since potential redistribution of NPs due to wash-down effects when filling the lung is avoided, while the airway diameters of deflated lungs should be corrected for deformation (shrinkage) effects from the bronchioles to the

alveoli due to the lack of cartilage. Moreover, lung shrinkage also occurs during tissue clearance, but this effect is expected to be limited to secondary bronchi and higher order generations due to the massive presence of cartilage in the trachea and primary bronchi. Data for originally measured and deflation-corrected diameters of the affected airways (secondary, tertiary bronchus, small bronchioles) and alveolar mean chord length (MCL) are presented in Figure 1d and e for both inflated and deflated lungs. The MCL in the inflated lungs filled with 0.8–1 mL of agar

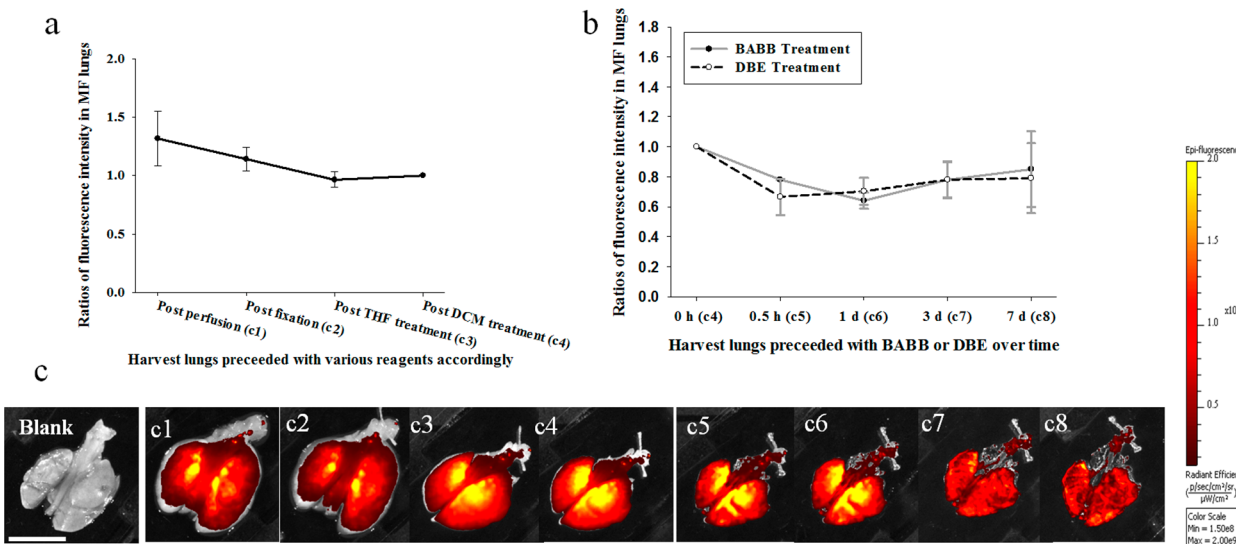


**Figure 2.** Analysis of fluorophore (MF NPs) stability in lungs at different stages of the 3DISCO optical clearance protocol using the *in vivo* imaging system (IVIS). The fluorescence intensity at each step was normalized to that after DCM treatment, starting after lung perfusion, over water and lipid removal (a) to refractive index matching with BABB or DBE (b). (c) Representative *ex vivo* lung images (c1–c8) from mice receiving 25  $\mu$ g of MF via intratracheal instillation measured by IVIS, indicating that the fluorescence of MF is relatively stable during the first day of the protocol and preserved up to 7 days (storage in BABB or DBE), despite the occurrence of lung shrinkage. The left lung of panel c (a, blank lung) represents no fluorescence can be observed under the same scale of NP-specific ex/em channel as the treated lung. Scale bar: 1 cm.

(corresponds to near full inflation of the lung) was determined to be  $49.7 \pm 10.9 \mu\text{m}$ , which agrees with the  $55.0 \pm 12.1 \mu\text{m}$  obtained from the deflated lung after applying the deformation correction due to the low inflation state. This MCL value is consistent with literature values ranging from 30 to 70  $\mu\text{m}$  in healthy adult mice for varying states of lung inflation.<sup>33,34</sup> Moreover, the branching angle of airway bifurcations averaged over all airway orders of four lungs was found to be  $55.0^\circ \pm 14.2^\circ$  (for W57BL/6 mice), which is consistent with the angles around  $10^\circ$  to  $100^\circ$  found in first six airway generations of C57BL/6 mice,<sup>35</sup> but slightly higher but less broadly distributed than  $45.6^\circ \pm 24.3^\circ$  observed in adult BALB/c mice using contrast-enhanced micro-CT.<sup>36</sup>

The paramount role of excellent lung perfusion for high-quality tissue clearance is evident from lung morphology images (autofluorescence channel). Residual blood due to poor transcardial perfusion of the lung will inhibit light penetration, resulting in “dark regions” near the center of the lung (Figure S1a). Since laser light with larger wavelength is less attenuated and therefore penetrates deeper into tissue, red (or near-infrared) light allows for more uniformly illuminated images of the 3D whole lung morphology, even for less than perfectly cleared lungs (Figure S1b,c). After surface rendering using Imaris, the airway structure becomes even more evident in the red than in the green channel (Figure S1d).

In summary, organic solvent-based clearing combined with LSFM imaging preserves the integrity of the lung architecture and thus offers the potential for providing higher accuracy 3D lung morphometry *versus* conventional sectioning-based, 2D stereological methods.

**Effects of Tissue Clearing on Fluorescence Stability of NPs.** In general, the 3DISCO clearing protocol involves tissue dehydration, lipid removal, and matching of the refractive index (RI), which is accomplished by treatment with three organic solvents, tetrahydrofuran (THF), dichloromethane (DCM), and dibenzyl ether (DBE). This rather harsh chemical treatment regimen could eradicate the activity of cell-produced flu-

rescence reporter dyes (*e.g.*, fluorescence proteins) and fluorescence-labeled NPs (*e.g.*, by digestion of the polystyrene latex matrix protecting the Sky Blue dye). In this study a time-saving and accurate method was developed for fast checking the stability of fluorescence dyes and tissue shrinkage during and after tissue clearing using an IVIS system, which allowed for *ex vivo* imaging of whole murine lungs before and after each step of the clearing procedure. This *ex vivo* imaging method is superior to standard *in vitro* incubation of fluorophores with each organic solvent, as fluorophores may not dissolve/disperse in and thus separate from organic solvents, leading to inaccurate and biased information. In this study, three types of fluorescent NPs with volume median diameters between 17.6 and 480 nm (Sky Blue (diameter:  $480.5 \pm 114.5 \text{ nm}$ ), melamine resin (MF) NPs ( $474.3 \pm 124 \text{ nm}$ ), and quantum dots (QDs,  $17.6 \pm 6.7 \text{ nm}$ , see Figure S2 for size distributions) were intratracheally instilled into mice, and lungs were harvested, perfused, and spectrophotometrically measured using the IVIS. This analysis of fluorophore stability revealed that the fluorescence intensity of MF NPs was statistically insignificantly decreased during tissue clearing and no significant difference was found between the mixture of benzyl alcohol and benzyl benzoate (BABB) and DBE treatment up to 7 days, indicating that the fluorescence activity of MF NPs is well preserved during the tissue clearing process (Figure 2a and b). Also, the fluorescence intensity of lungs instilled with MF and QDs at a dose of 62.5  $\mu\text{g}/\text{lung}$  and 40 pmol/lung, respectively, was over 10-fold higher than the autofluorescence of blank lungs in the NP-specific optical channels (Figure S3a and b), which provides a sufficient signal-to-background ratio for quantitative NP dosimetry with LSFM imaging as shown below. Moreover, long-term fluorescence stability of MF NPs after 3DISCO processing was observed for up to weeks and even months (Figure 2b and c). In contrast, Sky Blue was degraded *ca.* 150-fold (according to IVIS) by tissue clearing, resulting in signal-to-background ratios of about 1.5 even for a very high dose of 100  $\mu\text{g}/\text{lung}$ , which was too low for reliable NP dosimetry (data not shown). It is also noteworthy

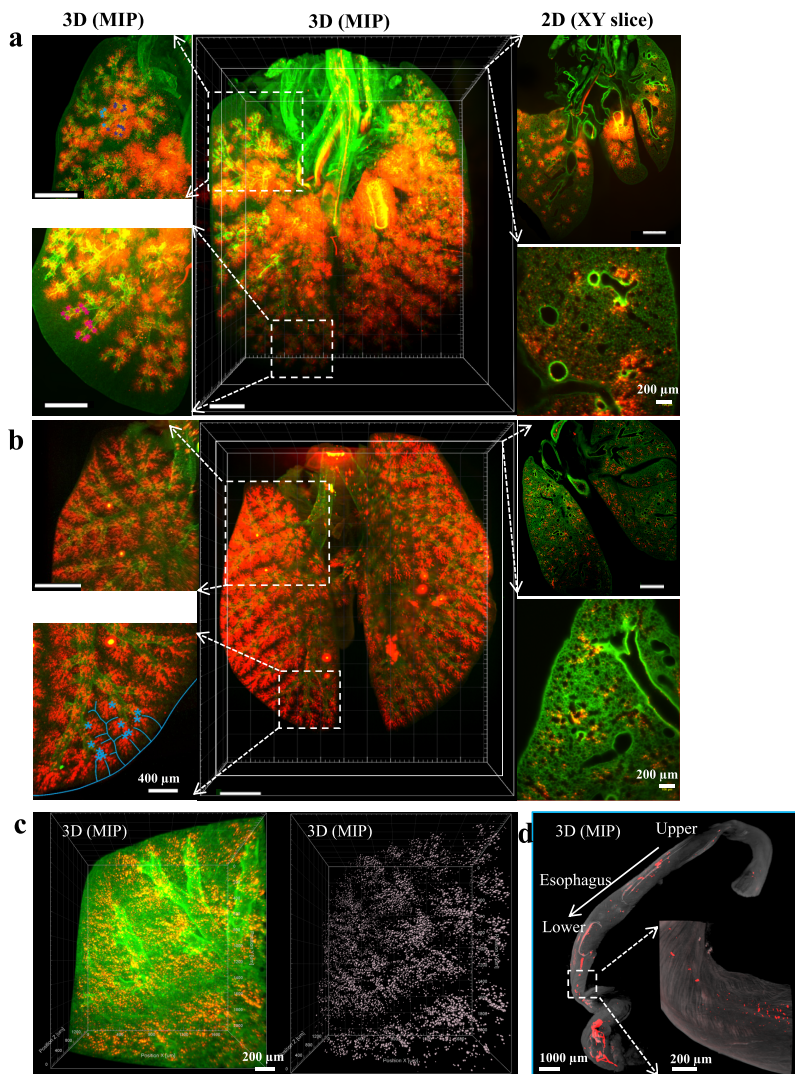


**Figure 3.** 3D mapping of melamine resin (MF) NP distribution pattern in (nondissected) whole murine lungs after pulmonary NP delivery *via* instillation and inhalation. Distribution of MF (red) in a Z-stack image of a whole lung (3D MIP) and in a single slice (2D *xy* slice) with respect to tissue structure (autofluorescence, green) after different application routes (panel a: instillation; panel b: inhalation). NPs are observed to accumulate along the whole bronchial tree and into the acini. A much more homogeneous NP distribution pattern was detected for inhalation (panel b) as compared to the patchier deposition pattern for instillation (panel a). After instillation preferential central acini were heavily loaded and relative homogeneously filled with NPs (dark blue asterisks in upper right panel of a), and most of the peripheral acini received only very small amounts of NP (magenta asterisks in lower right panel in a). After inhalation the deposited amount per acinus was much more homogeneous and similar in central or peripheral regions of the lungs (central panel in b). However, the NP deposition inside individual acini was very inhomogeneous: While the proximal regions received most of the NPs, the distal regions showed little deposition (light blue asterisks lower right panel in b). (c) At cellular resolution even for inhalation preferential proximal localization of NPs inside acini was further revealed (left) independent of the lung region, as illustrated by spot ( $5.5 \mu\text{m}$ ) rendering (right). (d) 3D visualization of MF (red) transported and accumulated in the esophagus (gray) immediately ( $<3$  min) after administration. Undesignated scale bars:  $1500 \mu\text{m}$ . The fluorescence intensity scale in the different images/panels varies for optimized overlay representation.

that the lungs shrunk after THF treatment by about 37–44% in the projected area with no further shrinkage after 1 day of DBE and/or BABB treatment (Figure S4).

**3D Lung Mapping of MF Distribution with Cellular Resolution after Intratracheal Instillation and Inhalation Application.** Numerous studies have been performed on NP–lung interaction after pulmonary delivery of NMs *via* intratracheal instillation and inhalation. However, potential differences in the distribution of NPs throughout the murine lung depending on the application route are still not sufficiently described. The specific capabilities of tissue clearance reduce tissue–light interactions (absorption, scattering) and allow for co-imaging of (label-free) lung morphology and particle

distribution throughout the entire murine lung with cellular resolution (tissue penetration of light is over a few centimeters). In particular, overlaying maximum intensity projection (MIP) images of the NP distribution with the 3D lung structure reveals insightful information regarding the NP deposition pattern. This can be seen in the representative images obtained after intratracheal instillation or inhalation of MF (Figure 3a and b). Not surprisingly, MF was found deposited along the bronchial tree starting from the trachea down to the terminal bronchioles and into the acini for both application routes (Figure 3 and Videos S2 and S3). An acinus is defined as the airways distal of the terminal bronchioles. In mice these are the alveolar ducts and sacculi distal of the bronchio–alveolar duct

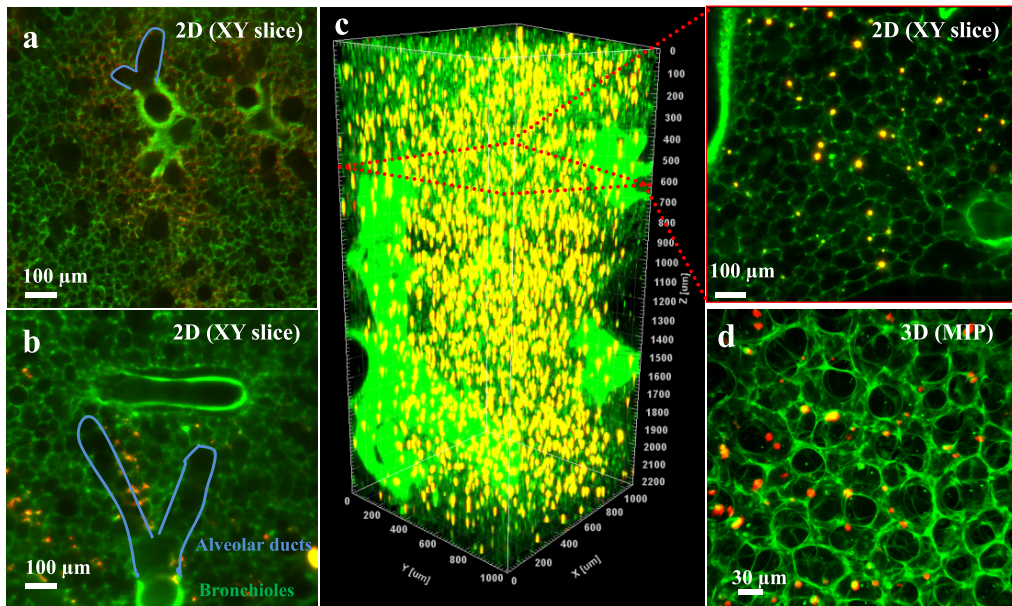


**Figure 4.** Visualization of NP deposition (red/yellow) with respect to alveolar tissue architecture (autofluorescence, green) at cellular resolution in deflated and inflated lungs. Cellular localization of MF NPs in the lungs scanned by LSFM, showing MF distributed into the terminal bronchioles (green), alveolar ducts (blue solid lines), and proximal alveoli of the acini immediately after both instillation (a) and inhalation (b). 3D images of MF distribution using LSFM (c) and confocal microscopy (d) at single-cell resolution in an inflated murine lung at 24 h after instillation, indicating the NPs were formed in relatively bigger agglomerates, which are likely due to phagocytic uptake and confinement by alveolar macrophages. LSFM allows for label-free deeper imaging of cleared tissue (z-direction: 2–5 mm) than confocal microscopy (50–80  $\mu$ m).

junction. The 3D distribution pattern of NPs in the airways and acini varied significantly for different application routes. Inhalation exhibited a much more homogeneous NP distribution pattern as compared to the patchier and preferentially central and upper airway and central alveolar deposition pattern for instillation (Figures 3a,b and S5). Moreover, for inhalation extremely high NP doses were deposited at the end of the trachea and in certain regions of the lower airways appearing as circular drops (*ca.* 100–200  $\mu$ m), which are possibly due to redistribution of deposited bulk liquid due to partial blocking of the airway (Figure S5). These features were not as evident for instillation application. When zoomed in or examined under higher magnification (Figure 3c), MF NPs were found to be mainly located in the small (or terminal) bronchioles but less accumulated in larger airways for both routes of delivery. Acinar deposition was quite different for the two forms of application. While after instillation the centrally located acini receive high doses, which were deposited all over the acini, the peripheral acini receive much lower doses, which were deposited in the entrance area of the acini (Figure 3a, as also shown by the central/peripheral scale; see below). After inhalation centrally and peripherally located acini received similar doses, which were predominately located in their proximal half (Figure 3b). Figure 4a and b shed more light on NP deposition in the alveolar septum and smaller bronchioles at cellular resolution after both applications. At this high level of resolution the NP distribution was not homogeneous in the alveolar region (inside acini). At 24 h after instillation we were able to visualize the 3D NP localization in intact lung tissue covering a volume of 1  $\times$  1  $\times$  2 mm<sup>3</sup> (and even bigger volumes like 5  $\times$  5  $\times$  5 mm<sup>3</sup> are possible, data not shown) without fading of fluorescence intensity as a result of highly reduced light attenuation in optically cleared tissue (Figure 4c and Video S4). Confocal imaging can also provide excellent label-free 3D images of NP distribution

(Figure 4d and Video S5), while it is limited by imaging depth (around 60  $\mu$ m) due to the low autofluorescence of alveoli (indistinct signal over lumen). The NPs had formed larger agglomerates 24 h after both applications as compared to NPs at 0 h (Figure 4 and Figure S6), which is likely due to phagocytic uptake and confinement by alveolar macrophages.<sup>37</sup> Spot rendering of MF with Imaris revealed an apparent average NP diameter of approximately 5.5  $\mu$ m immediately after inhalation (Figure 3c). This image analysis is unreliable for instilled NPs due to the patchy distribution of NPs in instilled lungs, limiting the localization of NPs by intensity gating. Moreover, existence of NPs in the esophagus indicated that NPs can be cleared within a few minutes toward the digestive tract by either mucociliary clearance or coughing (Figure 3d and Video S6).<sup>38</sup>

**Quantitative Analysis of Dose and Regional Deposition of Inhaled MF.** It became evident that each lung had a different autofluorescence level due to differences in the optical properties of the lungs, in lung volume, and LSFM instrument uncertainties (despite that the same settings of LSFM were used for all lungs). Here, the average of measured total fluorescence intensity from blank lungs was  $(11.1 \pm 3.33) \times 10^{10}$ , and the relatively high standard deviation of 30.2% demonstrates the variations in tissue-induced fluorescence due to lung and instrument variations. Therefore, the correction of the total fluorescence level in each NP-treated lung and subtraction of the lung-specific autofluorescence, which may also depend on the quality of tissue clearance, is a prerequisite for accurate dosimetry from LSFM data (details in SI Method 1). After correction, the average fluorescence signal from blank lungs was  $(10.2 \pm 1.84) \times 10^{10}$  with a standard deviation of 18%, representing the substantially improved measurement stability. Also, Figure 5a shows the linearity of a standard curve obtained from mice instilled with known NP doses ( $R^2 > 0.99$ ). This is further proven by the gradually enhanced mean fluorescence

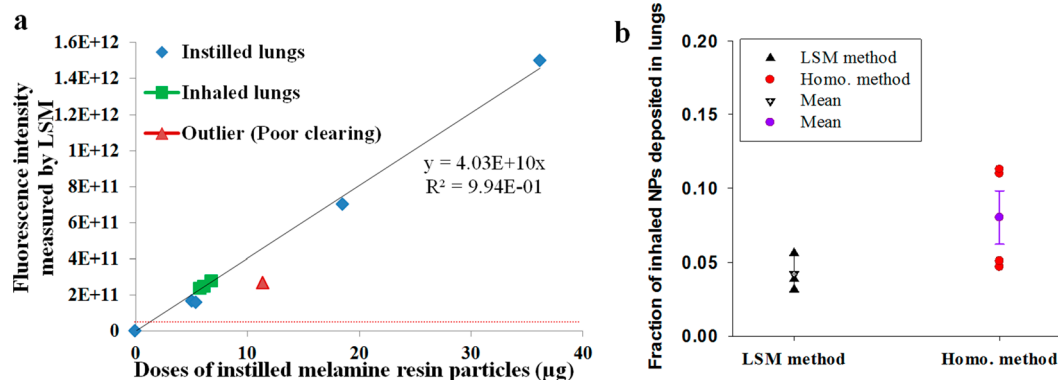


**Figure 5.** Establishment of the fluorescence intensity–dose correlation curve and quantitative dosimetry of inhaled doses in mouse lungs after inhalation. MF doses in inhaled lungs were determined from the linear fluorescence intensity–dose standard curve ( $R^2 = 0.99$ ) obtained from instilled lungs with known MF doses generated from all LSFIM slices of the lungs (a). Poor quality of optical tissue clearing mitigates the measured NP-induced intensity, which explains the outlier of the instilled lung. The limit of detection is defined as 3-fold standard deviation ( $3\sigma$ ) of autofluorescence about the mean autofluorescence level, which is represented by the red dashed line (a). The fraction of inhaled NPs deposited in lungs determined by the LSFIM method is in agreement with that from the standard fluorescence-based dosimetry method in lung homogenates (b). Abbreviations: homo: homogenization; LSFIM: light sheet fluorescence microscopy.

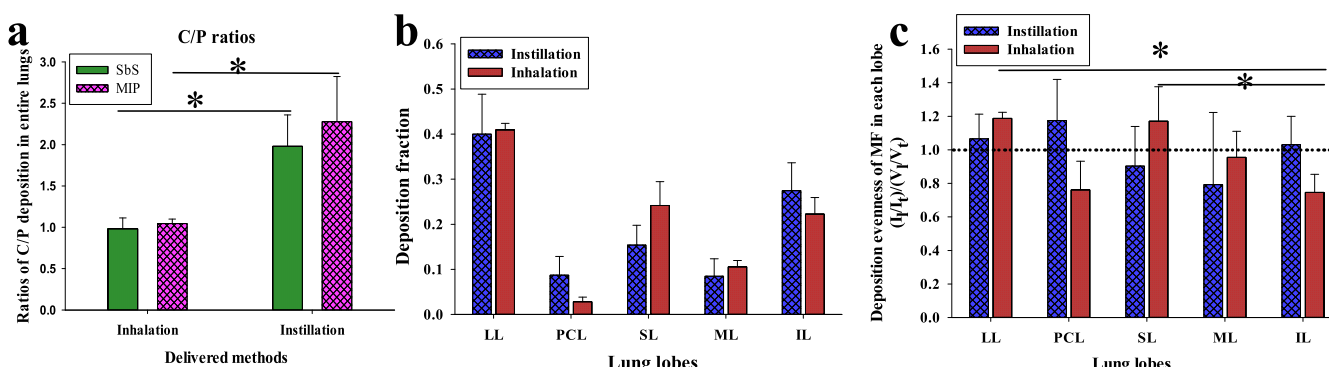


**Figure 6.** Quantitative analysis of MF spatial deposition in the lungs of mice after instillation and inhalation application routes. (a) Ratio of central to periphery (C/P) deposition analysis: C/P fluorescence intensity was normalized to the C/P area ratio. Lobewise deposition fraction (b, fractional MF dose in each lobe) and lobewise MF dose normalized to lobe volume (c) were analyzed for both application routes, showing that the variability in deposition fraction is consistent with lobe volume (ventilation volume). Abbreviations: SBS: slice by slice analysis; MIP: maximum intensity projection analysis of a whole lung; LL: left lung; PCL: postcaval lobe; SL: superior lobe; ML: middle lobe; IL: inferior lobe.

intensity in MIP images containing increasing doses of MF (12.5, 25, 50  $\mu$ g), as seen in Figure S5a. Poor clearing of tissue due to, for example, incomplete removal of blood during perfusion results in poor light penetration, and hence blurring reduced fluorescence intensity from the NPs, as seen as an outlier of the instilled lung in Figure 5a. The limit of detection is defined as 3-fold standard deviation ( $3\sigma$ ) of autofluorescence about the mean autofluorescence level, which serves as a zero point.<sup>39</sup> This yields a detection limit for MF of 1.37  $\mu$ g, where the  $3\sigma$  intensity level was converted into mass dose using the calibration curve shown in Figure 5a. Similarly, the autofluorescence-corrected intensity signal from inhaled lungs can be used to calculate the lung deposited dose. For these three lungs investigated here we found 5.96–7.01  $\mu$ g, which corresponds to  $4.2\% \pm 1.3\%$  of the inhaled dose (the dose in trachea was excluded). This value was not significantly different from the  $8.0\% \pm 1.8\%$ , which was measured by a more accurate dosimetry method utilizing tissue homogenization (Figure 5b).<sup>40</sup>

Quantitative assessment of the uniformity of NP distribution was performed on two scales, a central/peripheral scale (C/P; ca. 50%:50% in area) and a lobewise level, as described in the Materials and Methods section. The C/P ratio is widely used in clinical lung deposition studies using radiometric imaging.<sup>41</sup>

Here we found that inhalation resulted in a very uniform NP distribution as indicated by the C/P of  $0.98 \pm 0.13$ , while instillation was characterized by a 2-fold enhanced central deposition (C/P =  $1.98 \pm 0.37$ ) as determined by slice-by-slice analysis (Figure 6a). Interestingly, identical C/P ratios were obtained when analyzing not the whole slices of a Z-stack but only the MIP images overlayed onto the 2D projection of lung morphology (Figure S5). A more refined, lobewise analysis revealed that around 40% of the delivered NPs reached the left lung (single lobe) for both routes of application with larger variability for instillation. The remainder of about 60% deposited in the four lobes of the right lung with large lobe-specific variabilities (Figure 6b). These differences were largely consistent with differences in lobe volume (see Figure S7b for volume values). Especially instillation of NPs resulted in a volume-scaled NP distribution, as indicated by volume-normalized deposition fractions of unity within experimental uncertainties (Figure 6c). Similar results were found for inhalation of NPs, with somewhat larger deviations from unity, but still in agreement with unity for each lobe. In instilled lungs there was no significant difference in deposition fraction among all lobes, while in inhaled lungs there were elevated levels of NPs in the superior lobe and middle lobe relative to the

inferior lobe (**Figure 6c**). Fractional deposition of MF NPs in lung lobes and trachea (**Figure S7a**) for both application routes were also accomplished by this imaging method.

## DISCUSSION

Accurate and spatially resolved delivery of NPs in the lungs of animal models is essential for toxicological and drug efficacy studies. Depending on the site of delivery, NPs may induce different types and levels of biological response.<sup>2,9,38</sup> For instance, efficacy of a nanomedicine for lung emphysema requires delivery into the alveolar region (acini), while drugs for asthma may be more efficient if delivered to the conducting airways.<sup>42</sup> Unlike the bronchial region, the acini are considered more vulnerable against inhaled NPs since it is not protected by a thick mucus layer.<sup>43</sup> Moreover, the kinetics of NPs is known to be highly dependent on the site of deposition,<sup>44</sup> with alveolar deposition being conducive to translocation into the bloodstream and prolonged residence time in the lung.<sup>45,46</sup> In spite of the significance of NP distribution in the lung, currently available analytical methods are limited in terms of lung morphology characterization and/or NP dosimetry, especially on the whole-organ level.

The spatially resolved lung imaging method presented here addresses these issues by combining the reduction of light-tissue interactions *via* optical tissue clearing with LSFM. One of the key elements of this method is a clearing protocol for whole organs which has to be not only highly efficient with respect to time consumption and quality of optical transparency but also gentle enough to maintain tissue integrity and high quantum yield of fluorescent traces under the chemically harsh conditions of tissue clearance procedures. Here the 3DISCO<sup>25</sup> clearing protocol with modifications was used, as it was considered the most effective and time-saving organic solvent-based method (high degree of transparency within hours to days) among the recently developed optical tissue clearing methods including aqueous-based clearing methods (*e.g.*, CUBIC, SeeDB, FRUIT) and hydrogel-based clearing methods (*e.g.*, CLARITY, PACT/PARS).<sup>26</sup> Tissue clearing has been carried out in both human and animal lungs<sup>28,47</sup> for studies on, for example, the development of human embryo lung airways and branches<sup>48–50</sup> and macrophage infiltration in murine lung tumors.<sup>24</sup> However, there are only very few reports regarding the visualization of the distribution of NPs in intact (nonsliced) organs. For instance the CLARITY protocols have been applied to study NP localization in cleared organs other than lungs (*e.g.*, liver, spleen),<sup>31,51</sup> and NPs were found mainly retained inside the vessels of a small part of liver tissue (thickness: 1 mm). Compared to the protocols presented here, CLARITY protocols not only are more complicated and time-consuming (days to weeks) but also damage or partially destroy the structural integrity of the organ.<sup>52</sup> A general limitation of the tissue clearing technology is that it requires the availability of fluorescence proteins/biomolecules, dyes, and/or particles that maintain fluorescence intensity during the entire clearing protocol. For resilience testing of fluorescence tracers an easy-to-use and yet reliable *ex vivo* imaging method utilizing a low-resolution epifluorescence imaging system (IVIS) was introduced here for simultaneous testing of both fluorophore stability and tissue shrinkage/expansion during each step of the clearing protocol. In this study, three different types of NPs were tested, and metal- and resin-based NPs (QDs and MF) were found to be sufficiently stable, while polystyrene latex NPs lost their fluorescence intensity. Degradation or bleaching of fluorescence dyes can be

minimized by low-bleaching tissue clearing protocols (*e.g.*, aqueous-based clearing protocol CUBIC). There are more than 10 types of clearing protocols reported in the literature, but to the best of our knowledge most of them have not been tested for NPs, yet. We envision that *ex vivo* tissue imaging using IVIS will be a useful and robust method for selecting suitable dyes and determining tissue shrinkage/expansion during various clearing processes in future research. Moreover, this method may prove to be valuable for optimization of clearance protocols with respect to dye stability and tissue integrity.

Quantitative morphometry of the entire lung with high resolution is a challenge for both *in vivo* and *ex vivo* imaging modalities even for small animals such as mice. Simultaneous characterization of both the honeycomb arrangement of millions of alveoli and the intricate structure of the bronchial tree requires high resolution down to <10 μm combined with a large field of view up to centimeters for mice and up to tens of centimeters for humans. Basic structural parameters of the lung such as airway diameter and branching angle, MCL, and wall thickness are commonly used for diagnosing lung disease in both preclinical research and clinical settings.<sup>53</sup> For instance constricted airways are a hallmark of asthma, enlarged MCL indicates lung emphysema, and appearance of both features is known to be associated with chronic obstructive pulmonary disease (COPD).<sup>54,55</sup> By far the most widely used method for lung morphometry with cellular resolution is the design-based 2D stereological methods (histomorphometry and immunofluorescence).<sup>53</sup> This approach, typically performed in HE-stained lung sections under a light microscope, allows for quantitative measurements of MCL, alveolar surface to volume ratio, wall thickness, and other parameters using a coherent test line system based on point and intersection counting utilization of the computer-assisted stereological toolbox (CAST).<sup>33</sup> While this method offers colocalization of NPs and tissue structure at cellular resolution, it is time-consuming due to tissue slicing, staining, and slice-by-slice microscopy, resulting in at least partial loss of 3D information. For optically cleared and transparent murine lungs LSFM allows for planewise imaging of the entire, nondissected murine lung at high resolution within a relatively short period of time (tens of minutes to hours depending on resolution). Recently, X-ray-based computed tomography (CT) is widely used for morphometric analysis in both animal models and patients due to its noninvasive and time-saving procedures.<sup>36,56</sup> However, CT methods (*in vivo* or *ex vivo*) are limited in terms of resolution; they typically do not reach cellular dimensions except for *ex vivo* μCT imaging of fixed lung samples, with a resolution down to a few micrometers.<sup>57</sup> However, for animal models *ex vivo* LSFM imaging is much more conducive to bioactivity and functional imaging than μCT due to the much wider selection of probes with fluorescence activity than radioactivity. Thus, this study presents a label-free visualization of the entire 3D lung structure with cellular resolution and offers the morphometric analysis of both the entire bronchial tree and the alveolar structure in adult mice based on LSFM data. Airway morphometry and nerve populations in optically cleared lungs were previously visualized and computer modeled using immunostaining and BABB clearing by Scott *et al.*<sup>47</sup> However, the tissue deformation effect was ignored, which is essential for accurate lung morphological analysis due to the occurrence of lung deformation when the lung is out of the body (lower inflation state) and lung tissue shrinkage during BABB or 3DISCO clearing.<sup>28,58</sup> The validity of a tissue shrinkage factor correcting for changes in lung

morphology due to inflation state was verified by matching the airway diameters of collapsed, unfilled *ex vivo* lungs with agar-filled, almost fully inflated lungs. In addition, it was shown that the morphometric data on airway diameters (from first order,  $1048.5 \pm 94.0 \mu\text{m}$ , to fourth order,  $188.0 \pm 63.2 \mu\text{m}$ ), branching angle ( $55.0^\circ \pm 14.2^\circ$ ), and alveolar dimension (MCL:  $\sim 50 \mu\text{m}$ ) for WS7BL/6 mice are in good agreement with literature values.<sup>33,35,36</sup> Hence, tissue clearing and LSFM potentially provide the additional insights for whole lung morphometric analysis with cellular resolution including visualization and quantification of bronchial tree, alveolar sacs, and vasculature system. The use of tissue/cell-specific probes (*e.g.*, antibodies, dyes) may even allow for cell-specific imaging on the whole-lung level.<sup>30</sup>

This study further demonstrates that 3DISCO tissue clearing combined with multiwavelength LSFM allows for co-registration of NPs and lung morphology, thus yielding a 3D visualization of the NP distribution within the whole murine lungs at cellular resolution. The merit of this technique has been demonstrated by a comparison of the pulmonary NP distribution after instillation and inhalation of NPs. The accurate dosimetry of fluorescent NPs in the lung was obtained from LSFM data, as demonstrated by the linear dose–intensity curve obtained for instilled murine lungs with known NP doses. Application of this dose–intensity curve to lungs receiving an unknown NP dose *via* ventilator-assisted inhalation revealed that  $4.2\% \pm 1.3\%$  of the inhaled aerosol was deposited into the lungs, which is not statistically significantly different than the  $8.0\% \pm 1.8\%$  measured with an accepted reference method for lung dosimetry, namely, quantitative fluorescence analysis in lung homogenates.<sup>40</sup> Finally, LSFM images provided both qualitative and quantitative evidence for the expected finding that inhalation of aerosolized NPs results in more uniformly distributed pulmonary NP distribution than instillation. In addition to the obviously more patchy NP deposition in instilled lungs (Figure 3a and b) the quantitative analysis of the ratio of centrally and peripherally deposited NP dose showed that instillation resulted in about a 2-fold enhanced central deposition relative to peripheral deposition ( $C/P \approx 2$ ), while inhalation provided a uniform distribution of NPs ( $C/P \approx 1$ ). This is to be expected, since liquid bolus application is not expected to reach the peripheral lung regions as well as inhalation of aerosolized NPs, which is known to result in  $C/P$  ratios near unity not only in animal models but also in humans.<sup>41</sup> The order of NP deposition among lobes and *ca.* 40% inhaled aerosols reached in the left lung was determined by the lobewise deposition analysis, which is also consistent with the previous findings that used fluorescent (compressed) lung imaging.<sup>59,60</sup> Furthermore, after inhalation the acinar deposition showed a strong proximal to distal gradient, where roughly the proximal half received most of the NPs and the distal one much less to no NPs (Figure 3b). This pattern is of particular interest, because it was predicted by computational fluid dynamics simulations that the proximally located alveolar ducts serve as a filter for particles and strongly decrease any distal deposition.<sup>61</sup> Our data represent the visualizations of the predicted deposition pattern in living animals, and they verify the simulation *in vivo*. It is obvious that any uneven distribution of NP deposition is highly relevant for therapeutic and toxic effects. We note that some aspects of the NP deposition pattern reported here for mechanically ventilated, deeply anesthetized mice are likely to be different for nonventilated, spontaneously breathing or more mildly anesthetized mice, but the general trend of more spatially

uniform NP deposition *via* inhalation *versus* intratracheal instillation has also been found in spontaneously inhaling animals.<sup>59,60</sup>

These features represent substantial progress over previously used *in vivo* and *ex vivo* optical imaging modalities, which were mainly suitable for the semiquantitative determination of dose and biodistribution of NPs in the tissue due to limitations with respect to strong tissue autofluorescence and poor spatial resolution.<sup>9</sup> For example, cryo-slicing fluorescence imaging<sup>39</sup> can be used for quantitative dosimetry and 3D distribution in murine lungs, but with much worse resolution than possible with LSFM. Other nonoptical imaging techniques for detection of NP biodistribution, quantification, and biokinetics are available at the *in vivo* (*e.g.*, X-ray-based imaging, SPECT, PET, MRI) and *ex vivo* levels (*e.g.*, TEM, SEM, flow cytometry, 2D stereology), as summarized in recent reviews.<sup>2,9,21,62</sup> Application of those *in vivo* methods usually requires expensive instrumentation and the use of radiolabeling and/or contrast agents while providing limited spatial resolution. This greatly restricts observation of biological processes such as cellular uptake of NPs as well as generation of inflammation and reactive oxygen species, which is within reach of the method presented here. On the other hand, the *ex vivo* histological methods listed above allow for cellular resolution, but they are time-consuming, not suitable for whole-organ imaging, and insufficient for NP dosimetry. The imaging method for label-free lung morphometry analysis combined with quantitative NP distribution with cellular resolution on a tissue section overcomes some of these limitations, offering deep insights into 3D mapping of NP distributions in large tissue sections and organs with up to *ca.* 2 cm thickness, exceeding by far previously reported penetration depths.<sup>31</sup> Optical visualization of ultrafine NP and agglomerates (<100 nm diameter) is always challenging using fluorescence microscopy, as explained by two recent reviews.<sup>21,62</sup> We also note that not only fluorescence but alternative optical modalities such as light scattering can provide 3D imaging of metal NPs in intact and transparent tissues.<sup>63</sup> Future studies should exploit multiple staining probes for multifunctional biological response analysis with time-resolved LSFM to further refine this methodology for NP biokinetics, toxicology, and efficacy studies, facilitating the development of nanotoxicology and nanomedicine.

## CONCLUSION

In this study, we presented and validated an *ex vivo* whole-tissue imaging method for 3D quantitative co-visualization of (label-free) airway morphology and biodistribution of fluorescent nanoparticles with cellular resolution in murine lungs. Moreover, *ex vivo* whole murine lung imaging using epifluorescence imaging (here: IVIS) was introduced as a time-efficient and reliable method for analysis of the preservation of fluorescent dyes and lung morphology during the chemically harsh procedure of optical tissue clearing. Here 3DISCO tissue clearing and bispectral light sheet fluorescence microscopy were combined to co-visualize the label-free, entire 3D lung architecture (trachea to alveolar sacs) and pulmonary distribution of fluorescent NPs in nondissected, whole murine lungs (with an imaging depth of 1–2 cm for wavelengths of 500–750 nm). The method allows for quantitative NP dosimetry and reveals clear differences in the biodistribution of NPs applied to the lungs as bulk liquid suspension *via* intratracheal instillation or as a cloud of droplets (aerosol) *via* ventilator-assisted inhalation under anesthetized conditions on various resolution levels ranging from central-to-peripheral, to

lobewise, to cellular. Taken together, the approach presented here represents a robust method for single-modality analysis of combined 3D lung morphometry and quantitative biodistribution analysis of fluorescent probes (molecular, NP-bound) for the advanced analysis of biodistribution, biokinetics, and bioresponse analysis of NPs in whole murine lungs or whole-tissue sections and even small organisms.

## MATERIALS AND METHODS

**Materials.** Three types of commercial fluorescence-labeled NPs were used for the experiments, namely, polystyrene NPs with the embedded fluorescence dye Sky Blue (ex/em = 670 nm/710 nm; volume median diameter (VMD): 481 nm; Kisker Biotech GmbH, Steinfurt, Germany), MF fluorescence particles (MF, ex/em = 636 nm/686 nm; VMD: 474 nm, microParticles GmbH, Berlin, Germany), and Qdot 800 ITK carboxyl quantum dots (QDs with the maximum emission spectrum around 800 nm; VMD: 18 nm, Invitrogen, Ltd., Paisley, UK). The Syke Blue NPs (stock suspension: 10 mg/mL) were found to be unstable in the 3DISCO tissue clearing process and will therefore not appear in any of the images presented below. The MF NPs (stock suspension: 25 mg/mL) were prepared *via* an acid-catalyzed polycondensation reaction of melamine resin precondensates in the presence of selected fluorescent dyes in the aqueous phase. QDs (stock solution: 8  $\mu$ M) were made from the crystals of a semiconductor material (CdSeTe), shelled with a ZnS layer, and further coated with a polymer layer with carboxyl surface groups. Hydrodynamic diameter measurement of all three NPs was performed with dynamic light scattering (DLS) using a Malvern Zeta Sizer Nano instrument (Malvern Instruments Ltd., Malvern, UK).

**Animal Handling.** Mice were housed in individually ventilated cages (IVC-Racks; Bio-Zone, Margate, UK) supplied with filtered air in a 12 h light/12 h dark cycle (lights on from 06:00–18:00). The animals were provided with food (standard chow) and water *ad libitum*. All procedures involving animal handling and experiments were carried out in accordance with protocols approved by the Regierung von Oberbayern (District Government of Upper Bavaria).

Wild-type C57BL/6 mice (age 16–25 weeks, 6 males and 15 females, weight 20–30 g) were used for these experiments. Twenty-one mice were randomly divided into four groups: MF group (7 mice for instillation and 3 mice for inhalation); QDs group (3 female mice for instillation); Sky Blue group (3 female mice for instillation); and vehicle control group (3 females and 2 males without NPs treatment). For instillation, mice were anesthetized by the intraperitoneal injection of a ketamine and xylazine mixture and intubated by a nonsurgical technique using a 20G cannula inserted into the trachea, as previously described.<sup>39,64</sup> For intubated–ventilated inhalation exposure, the animals were deeply anesthetized by intraperitoneal injection with a triple combination of medetomidine (0.5 mg/kg bodyweight), midazolam (5 mg/kg bodyweight), and fentanyl (0.05 mg/kg bodyweight) and cannula intubated as described for instillation. The cannula was attached to a mechanical ventilator for mice (flexiVent system, SciReq Inc., Canada) to control their respiration during aerosol inhalation. The flexiVent was equipped with a nebulizer (Aeroneb Lab, small droplet diameter (2.5–4.0  $\mu$ m), Aerogen Inc., Ireland) for the generation of liquid aerosol droplets consisting of NP suspensions. For each mouse, the nebulizer was filled with 20, 40, or 60  $\mu$ L of a 12.5 mg/mL MF suspension (1:2 dilution of stock suspension) and the nebulizer was active for 40 ms per breath during ventilation of the mouse with 120 breaths/min, 400  $\mu$ L tidal volume, and an inhalation–exhalation time ratio of 2:1. The mouse was sacrificed immediately after NP application by exsanguination (to avoid clearance of NPs from the respiratory tract) and then transcardially perfused with 20 mL of 0.1 M phosphate-buffered saline (PBS) at room temperature for flushing out all of the blood from the lung. Subsequently, the perfusion liquid was switched to the fixation solution 4% paraformaldehyde (PFA) in 0.1 M PBS (10 mL) and then the whole lung plus the esophagus were removed and postfixed in 4% PFA overnight. The harvested organ was kept in 0.1 M PBS until further processing (imaging). Notably, 2 of 7 instilled mice were sacrificed at 24 h after application of MF NPs. Both mice were

transcardially perfused with 20 mL of 0.1 M PBS, and then their lungs were filled with 4% PFA for 2 h fixation *via* the cannula-intubated trachea. Subsequently, the PFA was withdrawn and refilled through the cannula with 0.8–1 mL of warm, 0.1 M PBS-equilibrated 2% agar, which was subsequently cooled to stiffen the lung tissue and thus maintain the inflated state of the lungs.<sup>54</sup>

**Ex Vivo Whole-Lung Imaging Using IVIS.** To examine the fluorescence stability of the NPs and the morphometric integrity of the lung during optical tissue clearance, an efficient, simple, and time-saving (less than 1 min for an *ex vivo* lung imaging) *ex vivo* imaging was performed using the IVIS (Lumina II, Caliper/PerkinElmer, USA). Briefly, the entire lung was placed on a holder located centrally in the IVIS with NP-specific excitation and emission filters (for Sky Blue and MF ex/em = 640 nm/Cy5.5 and for QDs ex/em = 640 nm/ICG) for various time points during the tissue clearance procedures. For each time point the fluorescence intensity and the 2D projected geometric area of the lung were determined from the fluorescence/white light images with the Living Imaging 4.0 software (Caliper). The variations in fluorescence intensity and the projected lung area (as a measure of lung morphometry) revealed the degree of resilience of the NPs against chemical degradation during the 3DISCO clearing protocol and morphometric stability (expressed as area shrinkage factor of lung), respectively.

**Tissue Clearing and 3D Imaging.** Whole-lung clearing was performed according to a modified version of the 3DISCO protocol.<sup>25</sup> Briefly, samples were dehydrated in 10 mL of 50% v/v tetrahydrofuran/H<sub>2</sub>O overnight (THF, Sigma 186562-1L), 50% THF/H<sub>2</sub>O 1 h, 70% THF/H<sub>2</sub>O 4 h, 80% THF/H<sub>2</sub>O 4 h, 100% THF 1 h, 100% THF overnight, and 100% THF 1 h with slight shaking. Samples were gently dried and then incubated in DCM (Sigma 270997-1L) around 30–40 min until they sank to the bottom of the 50 mL conical tube (Corning, Falcon 352070). Finally, samples were incubated without shaking in BABB, a mixture of 1:2 v/v benzyl alcohol (BA, Sigma 305197-1L) and benzyl benzoate (BB, Sigma B6630-1L), or in DBE (Sigma 108014-1KG) for at least 2 h until imaging and could then be stored in DBE/BABB at room temperature.

Whole-lung samples were imaged with an LSFM (Ultramicroscope II, LaVision Biotec) equipped with a sCMOS camera (Andor Neo) and a 2 $\times$  objective lens (Olympus MVPLAPO 2 $\times$ /0.5 NA) equipped with an Olympus MVX-10 zoom body, which provided zoom-out and -in ranging from 0.63 $\times$  up to 6.3 $\times$ . For whole lungs of mice treated with Sky Blue or MF NPs, light sheet scans were generated with 0.63 $\times$  zoom magnification (lens+zoom, 1.26 $\times$  actual magnification) with different excitation and emission bandpass filters (ex/em = 640(30) nm/690(50) nm for Sky Blue and MF NPs; ex/em = 640(30) nm/795(50) nm for QDs; ex/em = 545(30) nm/605(70) nm for tissue autofluorescence for lung morphology measurement) with a step size of 10 or 20  $\mu$ m depending on sample size. Samples were generally imaged with a exposure time of 150 ms, at 100% laser power (80% laser power only used when epifluorescence was overqualified) with the light sheet (thickness 4–24  $\mu$ m) at different *xy* widths and numerical apertures (NA) depending mainly on the magnification of the image. Samples were also imaged at magnifications of 8 $\times$  (Figure 3c) and 12.6 $\times$  (Figure 4) using a 4–5  $\mu$ m Z-step. The LSFM imaging time for a whole lung usually takes between tens of minutes and a few hours depending on various parameters including sample size (here stack size *ca.* 6–10 mm), magnification, light beam (dual or single), and step size. For refractive index matching, the imaging chamber of the LSFM was filled with BABB or DBE, the final clearing solvent used for tissue clearing.

**Image Processing and Analysis.** The images shown in the figures including single-slice images and maximum intensity projection (a method for 3D data visualization that displays only the voxels with maximum intensity along each optical ray passing through the image stack in the projection image<sup>65</sup>) images were processed by ImageJ (<https://imagej.nih.gov/ij/>). 3D volume images and movies with 3D manipulation were generated using Bitplane Imaris (<http://www.bitplane.com/imaris/imaris>). Lung morphometry such as airway diameter and bifurcation angle was manually segmented and calculated in 3D using Imaris. The alveolar MCL was estimated directly by setting

up random test lines consisting of solid lines and dashed lines superimposed on 2D images using ImageJ as described in the literature.<sup>33,53</sup> The airway diameters and MCL of unfilled lungs should be corrected for deformation effects due to tissue shrinkage during optical clearing and differences in inflation state of the lung. The (1D) shrinkage factor of the former (1.27 for collapsed lung), which was only applied to airspaces from the second-order bronchus to more distal regions (strong cartilage in more proximal regions), was determined from the square root of the 2D area shrinkage factor as measured from IVIS images of the lung before and after tissue clearing. The deflation correction factor, which was applied to the bronchioles and MCL, was determined from the volume ratio of the inflated (0.8 mL agar + 0.3 mL residual lung volume) and deflated lung (0.3 mL),<sup>59,60</sup> yielding 1.54 ( $= (1.1/0.3)^{1/3}$ ). So the total correction factor applied to the collapsed lung is 1.27 for second- and third-order bronchi and 1.96 ( $= 1.27 \times 1.54$ ) for bronchioles and MCL. Surface rendering of the mouse bronchial tree was derived from the autofluorescence signal of the airways of blank (unexposed) lungs in all ex/em channels, and spot rendering of NPs in Figure 3c with a filter size of 5.5  $\mu\text{m}$  were also prepared using Imaris.

**Establishment of the Intensity–Dose Standard Curve for NP Dosimetry.** Quantitative analysis of the images recorded by LSFM requires accurate assessment of various sources of error including instrument biases and variations of lung optical properties. In order to achieve reliable NP dosimetry, the absolute fluorophore intensity in each NP-treated lung was calculated following total fluorescence correction and subtraction of tissue-induced autofluorescence signal (for detailed descriptions see SI method 1). The dose of fluorescent NPs in a whole lung should be principally proportional to the sum of the absolute fluorescence intensities from all LSFM slices. The conversion factor of the corrected absolute fluorophore intensity to the fluorophore dose can be determined by preparing instilled lungs with known but different amounts of NPs (50  $\mu\text{L}$  of 1:200, 1:100, 1:50, and 1:25 dilutions of MF stock solution). After yielding the desired fluorescence intensity–dose conversion curve (here a linear relationship was obtained), quantitative measurement of the deposited dose in the lungs of mice *via* inhalation exposure could be achieved. The inhaled NP dose in the lungs of mice *via* intubated inhalation exposure was determined by differential gravimetric analysis of the nebulizer including connecting tubing to the mouse prior to and after nebulization (here  $36.0 \pm 8.5\%$  of invested dose can be inhaled), and but only a small fraction of inhaled dose can reach the lung (Figure 4b).

**C/P and Lobewise Distribution Analysis.** The regional deposition of NPs in the lung was investigated on two scales, a two-region (central and peripheral region) and a lobewise approach. For the clinically widely used two-region approach, the area-normalized NP dose in a central and peripheral area is determined from single lung slices added over all slices or from a maximum intensity projection of the entire lung. The central region is defined as the circumference-shaped matched inner 50% of each lung slice, and the entire lung area in each image (slice) was determined by intensity thresholding. Subtraction of the fluorescence intensity of the central region from that of the total lung region yields the peripheral lung intensity, and the ratio of central to peripheral intensity was analyzed after total fluorescence correction and subtraction of tissue autofluorescence (details in SI method 2) and then normalized to the respective areas according to

$$\text{C/P} = \frac{I_c/I_p}{A_c/A_p}$$

where  $I_c$  and  $I_p$  refer to the absolute NP fluorescence intensities from the central and peripheral regions of lung slices, respectively.  $A_c$  and  $A_p$  are the areas in the center and periphery, respectively. Slice-by-slice  $A_c$  and  $A_p$  analysis was performed on every fourth slice of each lung stack excluding the top and bottom slices of a stack, which contained predominantly peripheral regions. The overall C/P ratio determined by averaging over all analyzed slices indicates the homogeneity of the dose deposition. C/P close to unity denotes a homogeneous fluorophore

distribution in the lung, whereas C/P larger than unity indicates preferential central airway deposition.

Moreover, lobewise analysis was also performed to reveal the uniformity of NP distribution among lung lobes for both application routes. First, the entire region outside the lung was automatically set to zero (intensity thresholding), and then the region of interest representing the individual lobe was selected manually based on recognition of the space between two adjacent lobes. Subsequently, the fractional deposition of NPs on all five lung lobes and the trachea was obtained using ImageJ. Uniformity of MF deposition was described as volume- (lung/lobe volume estimated using the Cavalieri principle)<sup>66</sup> normalized intensity signal for each lobe after total fluorescence correction and lobe-specific subtraction of tissue autofluorescence. The volume-normalized deposition fraction is calculated from

$$\text{Dep}_v = \frac{I_l/I_t}{V_l/V_t}$$

where  $I_l$  and  $I_t$  refer to the NP-triggered fluorescence intensity from a specific lobe (here: 5 lobes) and the total lung, respectively. Analogous  $V_l$  and  $V_t$  are the volumes of a specific lobe and the total lung (without trachea), respectively.  $\text{Dep}_v$  is close to 1 if the NP dose reaching a specific lobe is equal to the fractional lung volume of this lobe. Values larger and lower than unity indicate preferential or reduced NP deposition in this specific lobe.

**Fluorescence-Based Analysis of NP Dose in Lung Homogenates.** As a reference method for NP dosimetry, we also determined the NP tissue burden in the total lung (all five lobes together), trachea, and esophagus according to a previously described method relying on quantitative fluorescence analysis in homogenized tissue.<sup>40</sup> In brief, tissue samples were homogenized in a homogenizer (Ultra Turrax, 20000 rpm) at a 1:10 (m/v) ratio of tissue to 0.1 M PBS buffer. A standard curve relating fluorescence intensity and NP concentration in lung homogenates was established by using a series of known doses of MF added into the homogenates of blank lung tissue allowing for quantification of the NP dose in the tissue.

**Statistical Analysis.** The statistical analysis was performed using SigmaPlot version 12.0 (Systat Software GmbH, Germany). Normality was determined using the Shapiro–Wilk test and a visual assessment of histograms. Comparison results from two groups for normally distributed and non-normally distributed data were carried out using a two-sided Student's *t* test and a Mann–Whitney rank sum test, respectively. Comparisons among multiple groups were performed using a one-way analysis of variance (ANOVA) followed by a pairwise multiple comparison procedures (Holm–Sidak method). All data were presented as mean  $\pm$  SD. Significances are defined as 0.05 ( $P < 0.05$ , \*) and 0.01 ( $P < 0.01$ , \*\*).

## ASSOCIATED CONTENT

### S Supporting Information

The Supporting Information is available free of charge on the ACS Publications website at DOI: 10.1021/acsnano.8b07524.

Videos on co-visualization of lung morphology and nanoparticle distribution (ZIP)

Additional information including video captions (PDF)

## AUTHOR INFORMATION

### Corresponding Author

\*E-mail: otmar.schmid@helmholtz-muenchen.de. Tel: +49-89-3187-2557. Fax: +49-89-3187-2400.

### ORCID

Lin Yang: 0000-0003-0469-9288

### Author Contributions

L.Y., A.F., W.M., Y.D., D.K., G.M., J.C.S., G.B., W.H., T.S., D.R., A.W., and O.S. conceived and designed experiments. L.Y., A.F., W.M., Y.D., and D.K. carried out experiments. A.F. and G.B.

assisted in imaging using light sheet microscopy and confocal microscopy, respectively. J.C.S. and W.M. contributed to the interpretation of imaging data. L.Y., A.F., and O.S. analyzed data and drafted the manuscript. All authors read and approved the final manuscript.

## Notes

The authors declare no competing financial interest.

## ACKNOWLEDGMENTS

This research was (partially) supported through the EU Horizon 2020 project SmartNanoTox, grant agreement no. 686098, and Swiss National Science Foundation, grant no. 310030\_175953. We thank the China Scholarship Council (CSC) for providing the fellowship for L.Y. (201506820008).

## REFERENCES

- (1) Wagner, V.; Dullaart, A.; Bock, A. K.; Zweck, A. The Emerging Nanomedicine Landscape. *Nat. Biotechnol.* **2006**, *24*, 1211–1217.
- (2) Pelaz, B.; Alexiou, C. H.; Alvarez -Puebla, R. A.; Alves, F.; Andrews, A. M.; Ashraf, S.; Balogh, L. P.; Ballerini, L.; Bestetti, A.; Brendel, C.; Bosi, S.; Carril, M.; Chan, W. C. W.; Chen, C. Y.; Chen, X. D.; Chen, X. Y.; Cheng, Z.; Cui, D. X.; Du, J. Z.; Dullin, C.; et al. Diverse Applications of Nanomedicine. *ACS Nano* **2017**, *11*, 2313–2381.
- (3) Ding, Y.; Kuhlbusch, T. A. J.; Van Tongeren, M.; Jimenez, A. S.; Tuinman, I.; Chen, R.; Alvarez, I. L.; Mikolajczyk, U.; Nickel, C.; Meyer, J.; Kaminski, H.; Wohlleben, W.; Stahlmecke, B.; Clavaguera, S.; Riediker, M. Airborne Engineered Nanomaterials in the Workplace—a Review of Release and Worker Exposure During Nanomaterial Production and Handling Processes. *J. Hazard. Mater.* **2017**, *322*, 17–28.
- (4) WHO. *WHO Guidelines on Protecting Workers from Potential Risks of Manufactured Nanomaterials*; Geneva, 2017; 94.
- (5) Lelieveld, J.; Evans, J. S.; Fnais, M.; Giannadaki, D.; Pozzer, A. The Contribution of Outdoor Air Pollution Sources to Premature Mortality on a Global Scale. *Nature* **2015**, *525*, 367–371.
- (6) Traboulsi, H.; Guerrina, N.; Iu, M.; Maysinger, D.; Ariya, P.; Baglole, C. J. Inhaled Pollutants: The Molecular Scene Behind Respiratory and Systemic Diseases Associated with Ultrafine Particulate Matter. *Int. J. Mol. Sci.* **2017**, *18*, 243.
- (7) Mura, S.; Nicolas, J.; Couvreur, P. Stimuli-Responsive Nanocarriers for Drug Delivery. *Nat. Mater.* **2013**, *12*, 991–1003.
- (8) Chan, W. C. W. Nanomedicine 2.0. *Acc. Chem. Res.* **2017**, *50*, 627–632.
- (9) Kunjachan, S.; Ehling, J.; Storm, G.; Kiessling, F.; Lammers, T. Noninvasive Imaging of Nanomedicines and Nanotheranostics: Principles, Progress, and Prospects. *Chem. Rev.* **2015**, *115*, 10907–10937.
- (10) Stoeger, T.; Takenaka, S.; Frankenberger, B.; Ritter, B.; Karg, E.; Maier, K.; Schulz, H.; Schmid, O. Deducing *in Vivo* Toxicity of Combustion-Derived Nanoparticles from a Cell-Free Oxidative Potency Assay and Metabolic Activation of Organic Compounds. *Environ. Health Perspect.* **2009**, *117*, S4–60.
- (11) Ganguly, K.; Ettehadieh, D.; Upadhyay, S.; Takenaka, S.; Adler, T.; Karg, E.; Krombach, F.; Kreyling, W. G.; Schulz, H.; Schmid, O.; Stoeger, T. Early Pulmonary Response Is Critical for Extra-Pulmonary Carbon Nanoparticle Mediated Effects: Comparison of Inhalation Versus Intra-Arterial Infusion Exposures in Mice. *Part. Fibre Toxicol.* **2017**, *14*, 19.
- (12) Bakand, S.; Hayes, A. Toxicological Considerations, Toxicity Assessment, and Risk Management of Inhaled Nanoparticles. *Int. J. Mol. Sci.* **2016**, *17*, 929.
- (13) Pacurari, M.; Lowe, K.; Tchounwou, P. B.; Kafoury, R. A Review on the Respiratory System Toxicity of Carbon Nanoparticles. *Int. J. Environ. Res. Public Health* **2016**, *13*, 325.
- (14) Choi, H. S.; Ashitake, Y.; Lee, J. H.; Kim, S. H.; Matsui, A.; Insin, N.; Bawendi, M. G.; Semmler-Behnke, M.; Frangioni, J. V.; Tsuda, A. Rapid Translocation of Nanoparticles from the Lung Airspaces to the Body. *Nat. Biotechnol.* **2010**, *28*, 1300–1304.
- (15) Schmid, O.; Stoeger, T. Surface Area Is the Biologically Most Effective Dose Metric for Acute Nanoparticle Toxicity in the Lung. *J. Aerosol Sci.* **2016**, *99*, 133–143.
- (16) Maynard, A. D.; Kuempel, E. D. Airborne Nanostructured Particles and Occupational Health. *J. Nanopart. Res.* **2005**, *7*, 587–614.
- (17) Miller, M. R.; Raftis, J. B.; Langrish, J. P.; McLean, S. G.; Samutrtai, P.; Connell, S. P.; Wilson, S.; Vesey, A. T.; Fokkens, P. H. B.; Boere, A. J. F.; Krystek, P.; Campbell, C. J.; Hadoke, P. W. F.; Donaldson, K.; Cassee, F. R.; Newby, D. E.; Duffin, R.; Mills, N. L. Inhaled Nanoparticles Accumulate at Sites of Vascular Disease. *ACS Nano* **2017**, *11*, 4542–4552.
- (18) Schmid, O.; Cassee, F. R. On the Pivotal Role of Dose for Particle Toxicology and Risk Assessment: Exposure Is a Poor Surrogate for Delivered Dose. *Part. Fibre Toxicol.* **2017**, *14*, 52.
- (19) Kreyling, W. G.; Hirn, S.; Möller, W.; Schleh, C.; Wenk, A.; Celik, G.; Lipka, J.; Schaffler, M.; Haberl, N.; Johnston, B. D.; Sperling, R.; Schmid, G.; Simon, U.; Parak, W. J.; Semmler-Behnke, M. Air-Blood Barrier Translocation of Tracheally Instilled Gold Nanoparticles Inversely Depends on Particle Size. *ACS Nano* **2014**, *8*, 222–233.
- (20) Yang, L.; Kuang, H.; Zhang, W.; Wei, H.; Xu, H. Quantum Dots Cause Acute Systemic Toxicity in Lactating Rats and Growth Restriction of Offspring. *Nanoscale* **2018**, *10*, 11564–11577.
- (21) Vanhecke, D.; Rodriguez-Lorenzo, L.; Clift, M. J. D.; Blank, F.; Petri-Fink, A.; Rothen-Rutishauser, B. Quantification of Nanoparticles at the Single-Cell Level: An Overview About State-of-the-Art Techniques and Their Limitations. *Nanomedicine* **2014**, *9*, 1885–1900.
- (22) Yang, L.; Kuang, H.; Zhang, W.; Aguilar, Z. P.; Wei, H.; Xu, H. Comparisons of the Biodistribution and Toxicological Examinations after Repeated Intravenous Administration of Silver and Gold Nanoparticles in Mice. *Sci. Rep.* **2017**, *7*, 3303.
- (23) Dawidczyk, C. M.; Kim, C.; Park, J. H.; Russell, L. M.; Lee, K. H.; Pomper, M. G.; Searson, P. C. State-of-the-Art in Design Rules for Drug Delivery Platforms: Lessons Learned from FDA-Approved Nanomedicines. *J. Controlled Release* **2014**, *187*, 133–144.
- (24) Cuccarese, M. F.; Dubach, J. M.; Pfirschke, C.; Engblom, C.; Garris, C.; Miller, M. A.; Pittet, M. J.; Weissleder, R. Heterogeneity of Macrophage Infiltration and Therapeutic Response in Lung Carcinoma Revealed by 3D Organ Imaging. *Nat. Commun.* **2017**, *8*, 14293.
- (25) Erturk, A.; Becker, K.; Jahrling, N.; Mauch, C. P.; Hojer, C. D.; Egen, J. G.; Hellal, F.; Bradke, F.; Sheng, M.; Dodt, H. U. Three-Dimensional Imaging of Solvent-Cleared Organs Using 3dIco. *Nat. Protoc.* **2012**, *7*, 1983–1995.
- (26) Feuchtlinger, A.; Walch, A.; Dobosz, M. Deep Tissue Imaging: A Review from a Preclinical Cancer Research Perspective. *Histochem. Cell Biol.* **2016**, *146*, 781–806.
- (27) Stelzer, E. H. K. Light-Sheet Fluorescence Microscopy for Quantitative Biology. *Nat. Methods* **2015**, *12*, 23–26.
- (28) Susaki, E. A.; Ueda, H. R. Whole-Body and Whole-Organ Clearing and Imaging Techniques with Single-Cell Resolution: Toward Organism-Level Systems Biology in Mammals. *Cell Chem. Biol.* **2016**, *23*, 137–157.
- (29) Renier, N.; Wu, Z.; Simon, D. J.; Yang, J.; Ariel, P.; Tessier-Lavigne, M. Idisco: A Simple, Rapid Method to Immunolabel Large Tissue Samples for Volume Imaging. *Cell* **2014**, *159*, 896–910.
- (30) Klingberg, A.; Hasenberg, A.; Ludwig-Portugall, I.; Medyukhina, A.; Mann, L.; Brenzel, A.; Engel, D. R.; Figge, M. T.; Kurts, C.; Gunzer, M. Fully Automated Evaluation of Total Glomerular Number and Capillary Tuft Size in Nephritic Kidneys Using Lightsheet Microscopy. *J. Am. Soc. Nephrol.* **2017**, *28*, 452–459.
- (31) Sindhwan, S.; Syed, A. M.; Wilhelm, S.; Glancy, D. R.; Chen, Y. Y.; Dobosz, M.; Chan, W. C. Three-Dimensional Optical Mapping of Nanoparticle Distribution in Intact Tissues. *ACS Nano* **2016**, *10*, 5468–5478.
- (32) Wallau, B. R.; Schmitz, A.; Perry, S. F. Lung Morphology in Rodents (Mammalia, Rodentia) and Its Implications for Systematics. *J. Morphol.* **2000**, *246*, 228–248.

- (33) Knudsen, L.; Weibel, E. R.; Gundersen, H. J.; Weinstein, F. V.; Ochs, M. Assessment of Air Space Size Characteristics by Intercept (Chord) Measurement: An Accurate and Efficient Stereological Approach. *J. Appl. Physiol.* **2010**, *108*, 412–421.
- (34) Soutiere, S. E.; Mitzner, W. On Defining Total Lung Capacity in the Mouse. *J. Appl. Physiol.* **2004**, *96*, 1658–1664.
- (35) Thiesse, J.; Namati, E.; Sieren, J. C.; Smith, A. R.; Reinhardt, J. M.; Hoffman, E. A.; McLennan, G. Lung Structure Phenotype Variation in Inbred Mouse Strains Revealed through *in Vivo* Micro-Ct Imaging. *J. Appl. Physiol.* **2010**, *109*, 1960–1968.
- (36) Counter, W. B.; Wang, I. Q.; Farncombe, T. H.; Labiris, N. R. Airway and Pulmonary Vascular Measurements Using Contrast-Enhanced Micro-Ct in Rodents. *Am. J. Physiol.-Lung C* **2013**, *304*, L831–L843.
- (37) Geiser, M. Update on Macrophage Clearance of Inhaled Micro- and Nanoparticles. *J. Aerosol Med. Pulm. Drug Delivery* **2010**, *23*, 207–217.
- (38) Kreyling, W. G.; Möller, W.; Holzwarth, U.; Hirn, S.; Wenk, A.; Schleh, C.; Schaffler, M.; Haberl, N.; Gibson, N.; Schittny, J. C. Age-Dependent Rat Lung Deposition Patterns of Inhaled 20 Nanometer Gold Nanoparticles and Their Quantitative Biokinetics in Adult Rats. *ACS Nano* **2018**, *12*, 7771–7790.
- (39) Barapatre, N.; Symvoulidis, P.; Möller, W.; Prade, F.; Deliolanis, N. C.; Hertel, S.; Winter, G.; Yildirim, A. O.; Stoeger, T.; Eickelberg, O.; Ntziachristos, V.; Schmid, O. Quantitative Detection of Drug Dose and Spatial Distribution in the Lung Revealed by Cryoslicing Imaging. *J. Pharm. Biomed. Anal.* **2015**, *102*, 129–136.
- (40) van Rijt, S. H.; Bolukbas, D. A.; Argyo, C.; Wipplinger, K.; Naureen, M.; Datz, S.; Eickelberg, O.; Meiners, S.; Bein, T.; Schmid, O.; Stoeger, T. Applicability of Avidin Protein Coated Mesoporous Silica Nanoparticles as Drug Carriers in the Lung. *Nanoscale* **2016**, *8*, 8058–8069.
- (41) Möller, W.; Felten, K.; Meyer, G.; Meyer, P.; Seitz, J.; Kreyling, W. G. Corrections in Dose Assessment of 99mtc Radiolabeled Aerosol Particles Targeted to Central Human Airways Using Planar Gamma Camera Imaging. *J. Aerosol Med. Pulm. Drug Delivery* **2009**, *22*, 45–54.
- (42) Dolovich, M. B.; Dhand, R. Aerosol Drug Delivery: Developments in Device Design and Clinical Use. *Lancet* **2011**, *377*, 1032–1045.
- (43) Button, B.; Cai, L. H.; Ehre, C.; Kesimer, M.; Hill, D. B.; Sheehan, J. K.; Boucher, R. C.; Rubinstein, M. A Periciliary Brush Promotes the Lung Health by Separating the Mucus Layer from Airway Epithelia. *Science* **2012**, *337*, 937–941.
- (44) Semmler-Behnke, M.; Takenaka, S.; Fertsch, S.; Wenk, A.; Seitz, J.; Mayer, P.; Oberdorster, G.; Kreyling, W. G. Efficient Elimination of Inhaled Nanoparticles from the Alveolar Region: Evidence for Interstitial Uptake and Subsequent Reentrainment onto Airway Epithelium. *Environ. Health Perspect.* **2007**, *115*, 728–733.
- (45) Kreyling, W. G.; Semmler-Behnke, M.; Seitz, J.; Scymczak, W.; Wenk, A.; Mayer, P.; Takenaka, S.; Oberdorster, G. Size Dependence of the Translocation of Inhaled Iridium and Carbon Nanoparticle Aggregates from the Lung of Rats to the Blood and Secondary Target Organs. *Inhalation Toxicol.* **2009**, *21*, 55–60.
- (46) Möller, W.; Felten, K.; Sommerer, K.; Scheuch, G.; Meyer, G.; Meyer, P.; Haussinger, K.; Kreyling, W. G. Deposition, Retention, and Translocation of Ultrafine Particles from the Central Airways and Lung Periphery. *Am. J. Respir. Crit. Care Med.* **2008**, *177*, 426–432.
- (47) Scott, G. D.; Blum, E. D.; Fryer, A. D.; Jacoby, D. B. Tissue Optical Clearing, Three-Dimensional Imaging, and Computer Morphometry in Whole Mouse Lungs and Human Airways. *Am. J. Respir. Cell Mol. Biol.* **2014**, *51*, 43–55.
- (48) Belle, M.; Godefroy, D.; Couly, G.; Malone, S. A.; Collier, F.; Giacobini, P.; Chedotal, A. Tridimensional Visualization and Analysis of Early Human Development. *Cell* **2017**, *169*, 161–173.
- (49) Susaki, E. A.; Tainaka, K.; Perrin, D.; Yukinaga, H.; Kuno, A.; Ueda, H. R. Advanced Cubic Protocols for Whole-Brain and Whole-Body Clearing and Imaging. *Nat. Protoc.* **2015**, *10*, 1709–1727.
- (50) Tainaka, K.; Kubota, S. I.; Suyama, T. Q.; Susaki, E. A.; Perrin, D.; Ukai-Tadenuma, M.; Ukai, H.; Ueda, H. R. Whole-Body Imaging with Single-Cell Resolution by Tissue Decolorization. *Cell* **2014**, *159*, 911–924.
- (51) Sindhwan, S.; Syed, A. M.; Wilhelm, S.; Chan, W. C. Exploring Passive Clearing for 3d Optical Imaging of Nanoparticles in Intact Tissues. *Bioconjugate Chem.* **2017**, *28*, 253–259.
- (52) Murray, E.; Cho, J. H.; Goodwin, D.; Ku, T.; Swaney, J.; Kim, S. Y.; Choi, H.; Park, Y. G.; Park, J. Y.; Hubbert, A.; Mccue, M.; Vassallo, S.; Bakh, N.; Frosch, M. P.; Wedeen, V. J.; Seung, H. S.; Chung, K. Simple, Scalable Proteomic Imaging for High-Dimensional Profiling of Intact Systems. *Cell* **2015**, *163*, 1500–1514.
- (53) Hsia, C. C.; Hyde, D. M.; Ochs, M.; Weibel, E. R. An Official Research Policy Statement of the American Thoracic Society/European Respiratory Society: Standards for Quantitative Assessment of Lung Structure. *Am. J. Respir. Crit. Care Med.* **2010**, *181*, 394–418.
- (54) Sanderson, M. J. Exploring Lung Physiology in Health and Disease with Lung Slices. *Pulm. Pharmacol. Ther.* **2011**, *24*, 452–465.
- (55) John, G.; Kohse, K.; Orasche, J.; Reda, A.; Schnelle-Kreis, J.; Zimmermann, R.; Schmid, O.; Eickelberg, O.; Yildirim, A. O. The Composition of Cigarette Smoke Determines Inflammatory Cell Recruitment to the Lung in Copd Mouse Models. *Clin. Sci.* **2014**, *126*, 207–221.
- (56) Barre, S. F.; Haberthur, D.; Cremona, T. P.; Stampanoni, M.; Schittny, J. C. The Total Number of Acini Remains Constant Throughout Postnatal Rat Lung Development. *Am. J. Physiol.-Lung C* **2016**, *311*, L1082–L1089.
- (57) Vasilescu, D. M.; Gao, Z. Y.; Saha, P. K.; Yin, L. L.; Wang, G.; Haefeli-Bleuer, B.; Ochs, M.; Weibel, E. R.; Hoffman, E. A. Assessment of Morphometry of Pulmonary Acini in Mouse Lungs by Non-destructive Imaging Using Multiscale Microcomputed Tomography. *Proc. Natl. Acad. Sci. U. S. A.* **2012**, *109*, 17105–17110.
- (58) Muhlfeld, C.; Hegermann, J.; Wrede, C.; Ochs, M. A Review of Recent Developments and Applications of Morphometry/Stereology in Lung Research. *Am. J. Physiol. Lung Cell Mol. Physiol.* **2015**, *309*, L526–L536.
- (59) Yi, D.; Price, A.; Panoskaltsis-Mortari, A.; Naqvi, A.; Wiedmann, T. S. Measurement of the Distribution of Aerosols among Mouse Lobes by Fluorescent Imaging. *Anal. Biochem.* **2010**, *403*, 88–93.
- (60) Yi, D.; Naqvi, A.; Panoskaltsis-Mortari, A.; Wiedmann, T. S. Distribution of Aerosols in Mouse Lobes by Fluorescent Imaging. *Int. J. Pharm.* **2012**, *426*, 108–115.
- (61) Hofemeier, P.; Koshyama, K.; Wada, S.; Sznitman, J. One (Sub-)Acinus for All: Fate of Inhaled Aerosols in Heterogeneous Pulmonary Acinar Structures. *Eur. J. Pharm. Sci.* **2018**, *113*, 53–63.
- (62) Drasler, B.; Vanhecke, D.; Rodriguez-Lorenzo, L.; Petri-Fink, A.; Rothen-Rutishauser, B. Quantifying Nanoparticle Cellular Uptake: Which Method Is Best? *Nanomedicine* **2017**, *12*, 1095–1099.
- (63) Syed, A. M.; Sindhwan, S.; Wilhelm, S.; Kingston, B. R.; Lee, D. S. W.; Gommerman, J. L.; Chan, W. C. W. Three-Dimensional Imaging of Transparent Tissues Via Metal Nanoparticle Labeling. *J. Am. Chem. Soc.* **2017**, *139*, 9961–9971.
- (64) Gotz, A. A.; Rozman, J.; Rodel, H. G.; Fuchs, H.; Gailus-Durner, V.; de Angelis, M. H.; Klingenspor, M.; Stoeger, T. Comparison of Particle-Exposure Triggered Pulmonary and Systemic Inflammation in Mice Fed with Three Different Diets. *Part. Fibre Toxicol.* **2011**, *8*, 1.
- (65) Brown, D. G.; Riederer, S. J. Contrast-to-Noise Ratios in Maximum Intensity Projection Images. *Magn. Reson. Med.* **1992**, *23*, 130–137.
- (66) Michel, R. P.; Cruz-Orive, L. M. Application of the Cavalieri Principle and Vertical Sections Method to Lung: Estimation of Volume and Pleural Surface Area. *J. Microsc.* **1988**, *150*, 117–136.